

2

Electron Backscatter Diffraction (EBSD) Technique and Materials Characterization Examples

Tim Maitland and Scott Sitzman

1. Introduction

The term “electron backscatter diffraction” (EBSD) is now synonymous with both the scanning electron microscope (SEM) technique and the accessory system that can be attached to an SEM. EBSD provides quantitative microstructural information about the crystallographic nature of metals, minerals, semiconductors, and ceramics—in fact most inorganic crystalline materials. It reveals grain size, grain boundary character, grain orientation, texture, and phase identity of the sample under the beam. Centimeter-sized samples with millimeter-sized grains, to metal thin films with nanograins may be analyzed. The nominal angular resolution limit is $\approx 0.5^\circ$ and the spatial resolution is related to the resolution of the SEM, but for modern field emission SEMs (FE-SEMs), 20 nm grains can be measured with reasonable accuracy [1]. The macroscopic sample size is dependent on the ability of the SEM’s stage and chamber to orient a sample at 70° tilt at an appropriate working distance, usually in the range 5 to 30 mm.

1.1. History

The discovery of the fundamental diffraction on which EBSD is based can be traced back to 1928, when Shoji Nishikawa and Seishi Kikuchi (Fig. 2.1) directed a beam of 50 keV electrons from a gas discharge on a cleavage face of calcite at a grazing incidence of 6° . Diffraction patterns were recorded on photographic plates placed 6.4 cm behind and in front of the crystal, respectively, normal to the primary beam. The patterns were described as “...black and white lines in pairs due to multiple scattering and selective reflection” [2] (Figs. 2.2 and 2.3).

Shinohara [3] and Meibohm and Rupp independently saw the same phenomenon shortly after Kikuchi. Boersch [4], in 1937, produced some excellent patterns (Fig. 2.4) on film. Boersch studied both transmission and backscatter Kikuchi patterns (at 20 kV, $\sim 5^\circ$ of incidence and up to 162° of acceptance angle) obtained from cleaved, polished, respectively, etched NaCl, KCl, PbS, CaCO_3 , CaF_2 , quartz, mica, diamond, Cu, and Fe surfaces.

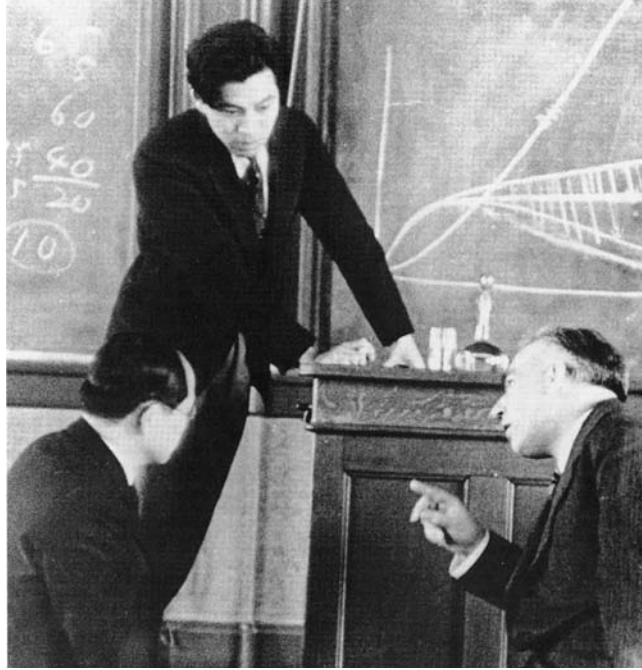


FIGURE 2.1. Seishi Kikuchi (*standing*). Thanks to Professor Shun Karato, Yale University, Geology Department. Originally published in *Scientific American*. Photo credit Nishina Memorial Foundation, courtesy of Hiroshi Ezawa.

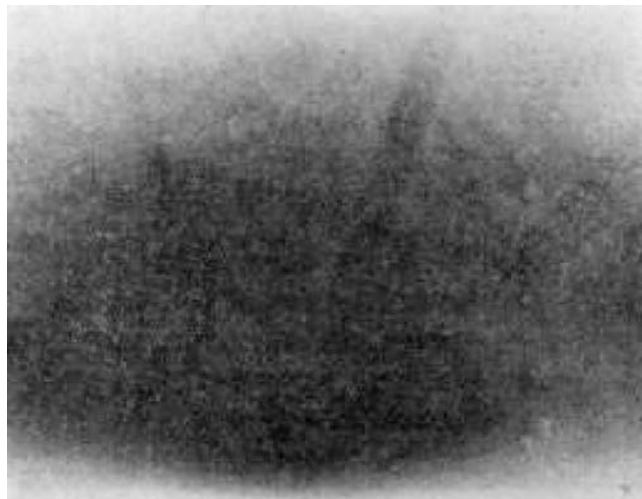


FIGURE 2.2. Kikuchi P-pattern from calcite cleavage.

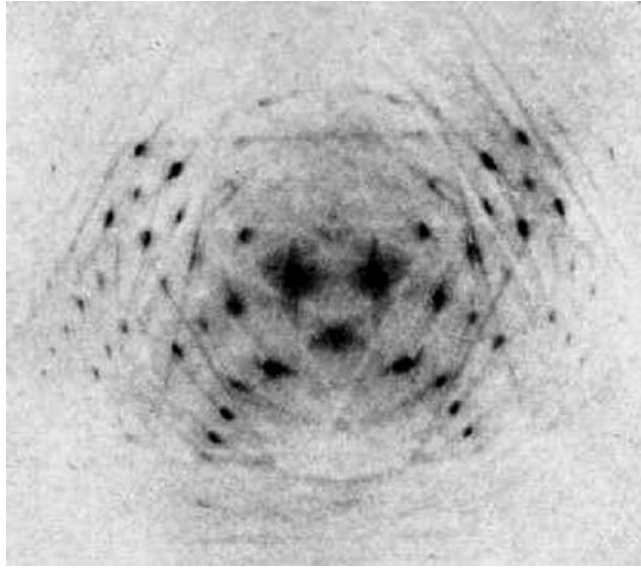


FIGURE 2.3. Kikuchi P-pattern from mica.

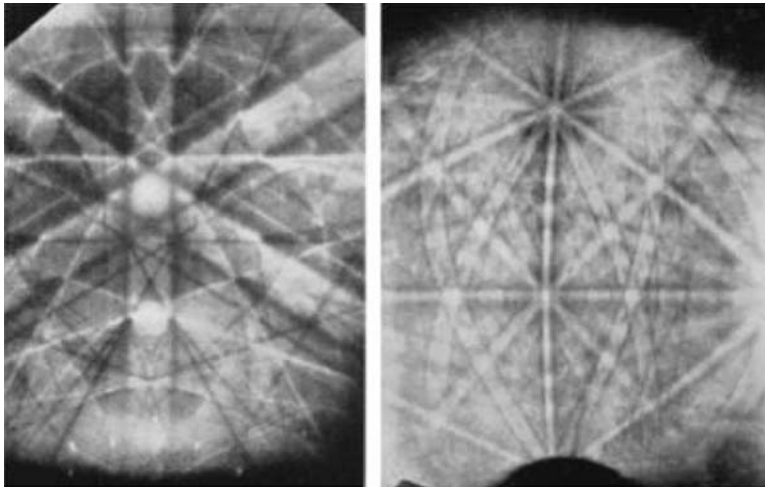


FIGURE 2.4. Boersch 1937 Iron Kikuchi patterns.

Alam et al. [5] in 1954 published their paper entitled “High-Angle Kikuchi Patterns.” Both Boersch and Alam et al. used purpose-built vacuum chambers for their work.

The introduction of the commercial SEM, in 1965, allowed greater progress during the decade 1969–1979 with three notable discoveries: selected area channeling

patterns (SACP) by Joy et al. at Oxford [6], Kossel diffraction by Biggin and Dingley at Bristol [7], and electron backscatter patterns (EBSP) by Venables and Harland at Sussex [8], the latter where a phosphor screen and TV camera were first used to record the patterns. The term used by Venables, EBSP, has been universally adopted today to refer to the Kikuchi pattern used in an EBSD system. Figure 2.5 shows an early EBSP from Venables [9], showing the ingenious method used to determine the pattern center, critical to accurate analysis of the pattern. The pattern center is defined as the shortest distance from point where the beam strikes the sample to the phosphor screen of the camera. Here Venables arranged three spheres inside the chamber between the sample and the camera. The shadows of the spheres projected onto the camera were elliptical and their major axes could be extrapolated. The intersection of these lines defined the pattern center.

The cross shows the position of the pattern center as predicted by current computer software. Figure 2.6 shows the solution to this EBSP, where the orientation of the BCC cubic unit cell is shown.

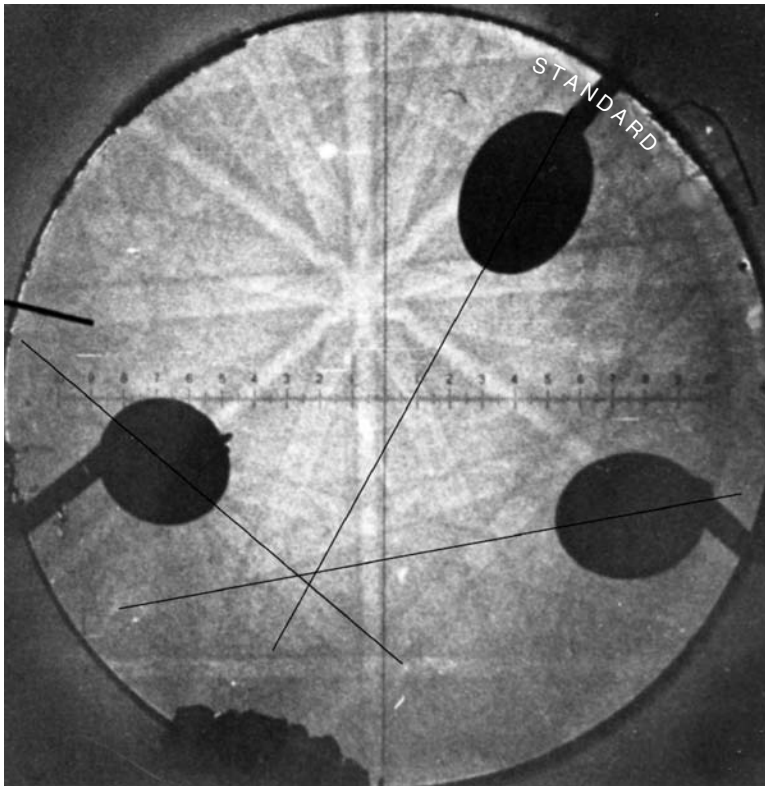


FIGURE 2.5. Venables' early EBSP showing elliptical shadows of spheres placed between the sample and the recording TV camera. The intersection of the black lines shows the empirically measured location of the pattern center.

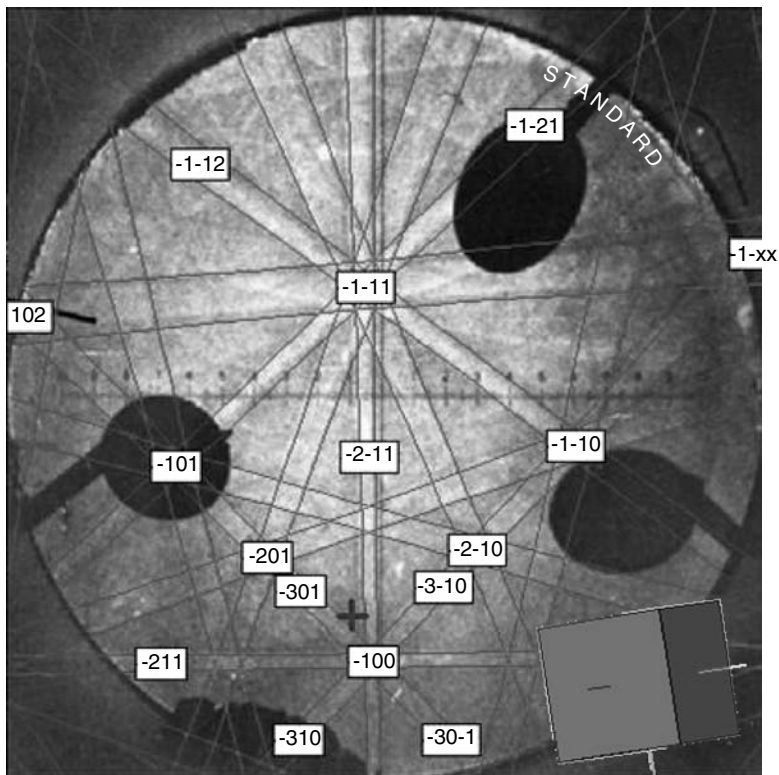


FIGURE 2.6. Venables' early EBSD indexed by modern software. The cross shows the computed location of the pattern center. Graphic inset shows approximate orientation of the crystal with respect to the sample surface.

In 1984, Dingley continued Venables earlier work with a phosphor screen and TV camera but added computer-aided indexing. This was a major step forward and became the model for modern-day EBSD systems.

In 1986, Niels Schmidt (Denmark) wrote software to index electron-channeling patterns (ECP) for all seven-crystal systems when he was a student at Aarhus University, before he went to Risoe National Laboratories. The year 1986 also saw the launch of the first commercial product by Link Analytical (now Oxford Instruments) using Dingley's software and hardware.

ECPs were limited to a spatial resolution of about 10 μm ; were difficult to implement (the SEM needed the ability to rock the beam about a point without the need for post lens deflection coils); and were slow. Schmidt adapted his general indexing solution for ECP along with the Dingley/Venables CCD technique to create software to index all seven-crystal systems using EBSPs instead. With this, he founded HKL Technology in 1990.

In 1992, Schmidt's colleagues Krieger-Lassen, Conradsen, and Juul-Jensen made one of the most important breakthroughs in the utility of this technique, the

use of the Hough transform. Without this, the ability to automatically detect bands reliably would not be available, relegating the technique to a slow, manual process. The Hough transform was developed in 1962 by Hough [10] as part of a patent to track high-energy particles [11]. Krieger-Lassen et al. used it to automatically identify Kikuchi bands in EBSPs.

In 1993, Brent Adams of Yale coined a new term, orientation imaging microscopy (OIM), to describe the technique of creating an orientation map (OM) of a sample. This is analogous to an EDX map, where instead of using color to represent the spatial distribution of each element present in the sample, it is used to show points of similar orientation.

Shortly thereafter, Dingley and Adams founded TexSEM Laboratory (TSL) in Utah. Thermo (then Noran) were retained to distribute the TSL system, and were responsible for significant numbers in the USA and Japan.

When Dingley and Adams formed TSL, Link/Oxford continued by offering their own EBSD system, as is the case today.

In 1999, EDAX acquired TSL as a part of their strategy to expand their line of analytical instruments. At this time, Thermo Noran had to look elsewhere for an EBSD solution. They turned to two independent players: Robert Schwarzer, of TU Clausthal, who had developed an independent solution for orientation and texture measurements, and Joe Michael, a pioneer of Phase Identification using EBSD at Sandia National Laboratory. Dingley had proposed using EBSD for phase identification in 1989, but Michael and Goehner coupled a slow-scan, high resolution CCD camera to their SEM to obtain sufficient resolution to aid in the indexing of patterns from unknown phases. In this technique, a database of possible phases is used to index the patterns, with the unknown phase being considered identified as the phase from the database that best fits the experimental pattern. Filtering of the database using chemistry and *d*-spacing is often used to reduce the number of candidate phases to a reasonable number on which to run the indexing algorithm.

Jarle Hjelen, Trondheim, Norway, created many camera designs over these years increasing in sensitivity and speed. Combining his cameras and Schmidt's software, HKL became a key supplier of EBSD systems especially to the geological sciences community who required the low-symmetry indexing algorithms of Schmidt for their mineral studies.

John Sutliff's pioneering work in the industrial application of the EBSD technique at GE Schenectady should not go unmentioned. Using HKL software, Sutliff was one of the first to see the practical utility of the technique in a modern industrial R&D environment.

1.2. How It Works?

EBSD operates by arranging a flat, highly polished (or as-deposited thin film) sample at a shallow angle, usually 20° , to the incident electron beam (Fig. 2.7) (since the SEM stage is often used to tilt the plane of the sample to this shallow angle, the value of stage tilt is often referred to and is typically 70°). With an

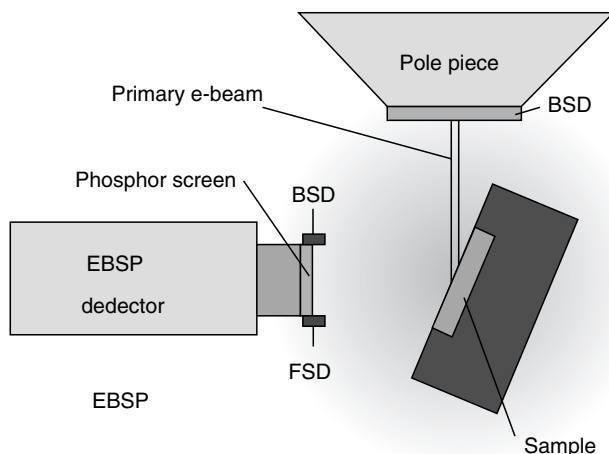


FIGURE 2.7. Schematic arrangement of sample orientation in the SEM. (Adapted from [13].)

accelerating voltage of 10–30 kV, and incident beam currents of 1–50 nA, electron diffraction occurs from the incident beam point on the sample surface. With the beam stationary, an EBSD pattern (EBSDP) emanates spherically from this point.

When the primary beam interacts with the crystal lattice (Fig. 2.8) low energy loss backscattered electrons are channeled and are subject to path differences that lead to constructive and destructive interference. If a phosphor screen is placed a short distance from the tilted sample, in the path of the diffracted electrons, a diffraction pattern can be seen. There are several discussions of the electron interactions involved; in particular Wells, “Comparison of Different Models for the Generation of Electron Backscattering Patterns in the SEM,” *Scanning* 21, 368–371 (1999) gives a good descriptions of the competing theories.

The spatial resolution of the technique is governed by the SEM electron optics as in conventional backscattered electron imaging. For high resolution imaging on nanograins, high-performance FE-SEMs are required, along with small samples and short working distances.

The EBSD detector attaches to a free port on the SEM chamber. Ideally, the port will be orthogonal to the stage tilt axis so that the sample may easily be tilted toward the detector at $\approx 70^\circ$, although other orientations are possible. Typically, the port will allow the detector to have a nominal working distance of ~ 20 mm, since a highly tilted sample necessitates moderate working distances. For small samples, shorter WDs may be attained if the EBSD detector and SEM port allows close proximity to the objective lens. Special detectors are available for less favorable port positions.

The detector is in fact a digital camera. Its CCD chip is illuminated by the phosphor screen that intersects the spherical diffraction pattern. The phosphor

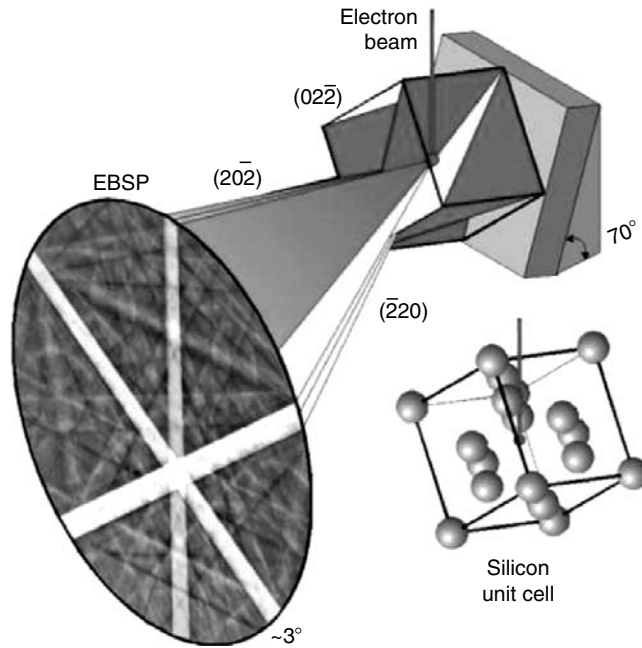


FIGURE 2.8. Electron interaction with crystalline material. (Adapted from [13].)

converts the diffracted electrons into light suitable for the CCD camera to record. With a stationary beam on a point on the sample, an EBSP (Fig. 2.9) is analyzed and in some cases stored. The EBSP is uniquely defined by the lattice parameters of the particular crystal under the beam; by the crystal's orientation in space; the wavelength of the incident electron beam (which is proportional to the acceleration voltage) and the proximity of the EBSP detector to the sample.

Specialized computer software analyzes the EBSP by detecting a number of Kikuchi bands using an optimized Hough transform. With a *priori* information about the candidate phases under the beam, the software determines all possible orientations with each phase and reports the best fit as the identified phase and orientation. The EBSP is then considered indexed when its orientation and phase are known.

Most SEMs are equipped with EDX spectrometers for chemical analysis by characteristic x-rays produced by the incident electron beam. Today, EDX systems take control of the beam location on the sample using the external scan interface on most SEMs (Fig. 2.10). EBSD requires the same interface to the SEM and thus, for most retrofits to existing systems, a simple electronic method to share this external interface is required. An intelligent switch box is placed between the EDX and the SEM and this arbitrates between the EDX and EBSD systems' access to the SEM. In addition to beam control, for large sample area coverage, integrated stage motion is required. SEM motorized stages are often accessible

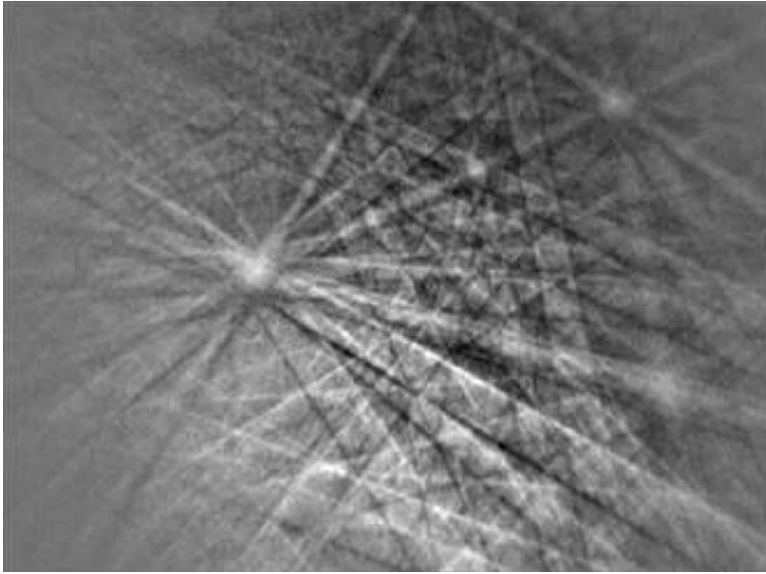


FIGURE 2.9. Example EBSP from Quartz.

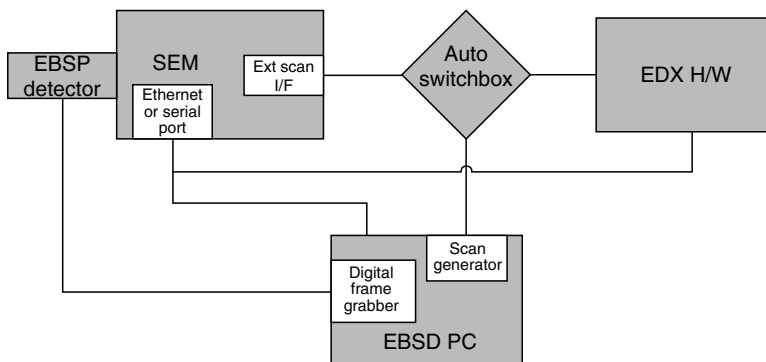


FIGURE 2.10. Schematic of SEM interface.

through an RS232 serial computer interface or Ethernet connection, which can be addressed by the operating software.

As the technique has developed in automated accuracy and overall speed, the ability to scan the beam over multiple points on the sample to create an OM has become practical, and is now the most common method for a microstructural investigation with EBSD. A map is defined by its location, size, and by the sampling step size between points. In this way, the resolution of the map may be adjusted to reveal the grain structure and grain boundary character, depending on the electron beam resolution under the sampling conditions, time available and

size of the sample area required. Improvement in speed has been made over the years, from manual indexing rates to 100 automatically indexed patterns/second (Fig. 2.11) [12]. The rate of change approximates an exponential increase since inception (Fig. 2.12).

Detectors used in normal SEM imaging produce a single dimensional output signal. With the beam at a given point on the sample, a signal is recorded and interpreted as the brightness in the output image. However, EBSD gives rise to a 3D pattern emanating from a point that is recorded in 2D on the phosphor screen.

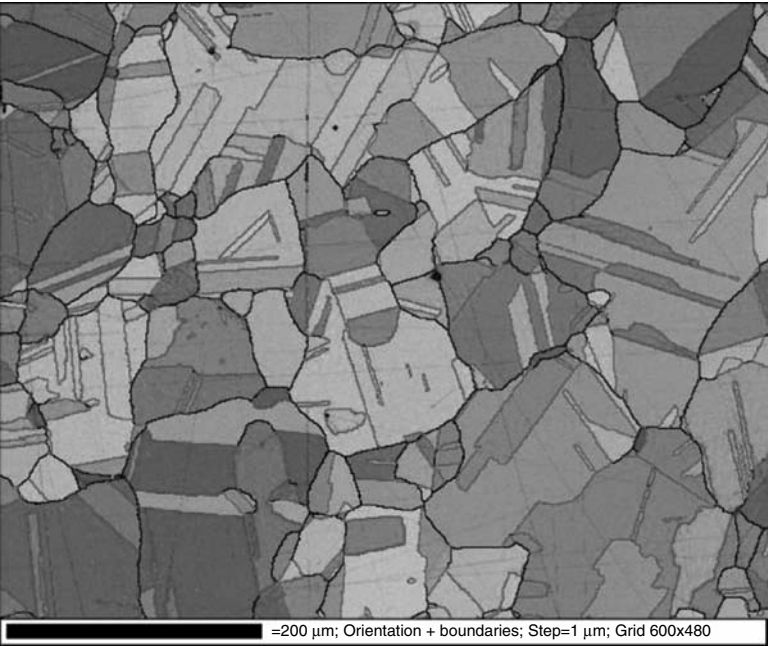


FIGURE 2.11. Brass map acquire at 100 indexed datapoints per second. (Adapted from [12].)

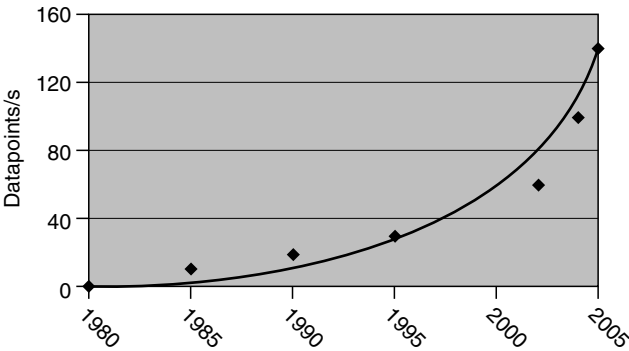


FIGURE 2.12. Mapping speed by year.

Hence, for every point analyzed on a sample, a 2D image of the diffraction pattern is analyzed. Imagine that a 512×512 pixel sample area is analyzed using EBSFs of $512 \times 512 \times 8$ bit pixels in size, $= 512^4 = 64$ GB of uncompressed raw data for one map! In practice, this amount of information is not always stored. Only the position, phase, orientation and some data quality information are stored at each point.

2. Data Measurement

As can be seen in Fig. 2.13, the data set produced by scanning the beam in a regular grid over the sample is comparatively simple. It is a simple database of measurements with each row being a point in the map and each column one of several measured parameters. To create this database, the beam is steered to each pixel point in the map. An EBSF is captured, analyzed, and either the phase and orientation derived or a zero-solution recorded, if the system was unable to measure the orientation. Zero-solutions can come from points where no EBSF is available, where overlapping EBSFs cannot be resolved, or when a new phase is encountered. EBSFs may not be produced when the sample surface deformation is so high that there is no coherent diffraction or when a noncrystalline material is encountered. Overlapping EBSFs occur at grain boundaries when the electron beam diameter is large enough to produce EBSFs from two grains simultaneously. When an EBSF can be solved, its Phase, XY position, orientation, goodness of fit, pattern quality, and other values are recorded.

2.1. Phase

If more than one match unit has been specified by the user, the best fit is listed here. Each match unit contains the information necessary to model the EBSF produced by the expected phase in the sample. The best fit between each match unit

Record Browser for Project [Alumin]											
Orientations											
Index	Phase	X (μm)	Y (μm)	Φ ₁ (°)	Φ ₂ (°)	Φ ₃ (°)	MAD (°)	OI	BC	BS	Status
1	Aluminum	0	0	17.88	30.14	66.90	0.500	0.000	225	68	6 bands detected
2	Aluminum	0.7	0	18.13	30.54	66.99	0.400	0.000	220	72	6 bands detected
3	Aluminum	1.4	0	17.98	30.18	66.73	0.300	0.000	227	70	6 bands detected
4	Aluminum	2.1	0	18.28	30.53	66.73	0.400	0.000	219	64	6 bands detected
5	Aluminum	2.8	0	17.89	30.38	67.06	0.700	0.000	226	57	6 bands detected
6	Aluminum	3.5	0	18.30	30.35	66.78	0.800	0.000	194	48	6 bands detected
7	Zero solution	4.2	0	0.00	0.00	0.00	0.000	0.000	156	38	Indexing not possible
8	Aluminum	4.9	0	357.49	33.71	88.25	0.700	0.000	189	48	6 bands detected
9	Aluminum	5.6	0	357.21	33.63	88.49	0.400	0.000	218	56	6 bands detected
10	Aluminum	6.3	0	356.79	33.52	88.58	0.600	0.000	223	60	6 bands detected
11	Aluminum	7	0	357.12	33.43	88.53	0.700	0.000	231	58	6 bands detected
12	Aluminum	7.7	0	357.38	33.59	88.49	0.600	0.000	228	59	6 bands detected
13	Aluminum	8.4	0	357.06	33.83	88.63	0.400	0.000	232	62	6 bands detected
14	Aluminum	9.1	0	357.03	33.65	88.40	0.400	0.000	233	61	6 bands detected
15	Aluminum	9.8	0	356.90	33.53	88.65	0.500	0.000	237	59	6 bands detected
16	Aluminum	10.5	0	357.01	33.80	88.69	0.500	0.000	242	60	6 bands detected
17	Aluminum	11.2	0	357.12	33.71	88.39	0.600	0.000	232	57	6 bands detected
18	Aluminum	11.9	0	356.82	33.65	88.58	0.600	0.000	192	48	6 bands detected
19	Aluminum	12.6	0	89.25	11.84	74.29	1.000	0.000	169	36	5 bands detected
20	Aluminum	13.3	0	89.64	12.07	73.32	0.500	0.000	216	43	6 bands detected

FIGURE 2.13. Database of mapped datapoints.

and the experimental EBSD determines the phase and orientation of the point on the sample under the beam.

2.2. Match Unit

A lookup table is used to match the experimental data to a set of crystallographic lattice planes with similar characteristics during crystallographic indexing. The match unit contains the crystallographic indices of Bragg-diffracting lattice planes (“reflectors”), the interplanar angles, the lattice spacing (d) and the intensity of the particular reflectors. The “match unit” is produced utilizing the Kinematical electron diffraction model and contains the following crystallographic parameters:

hkl : The crystallographic indices of Bragg-diffracting lattice planes (“reflectors”).

d_{hkl} : The lattice plane spacing of the particular reflectors.

n_{hkl} : The normal vectors to the reflectors.

I_{hkl} : The intensity of the reflectors.

n_i, n_j : The interplanar angles between the reflectors.

From these parameters the interplanar angles (n_i, n_j) are primarily used for indexing. The lattice plane spacing (d_{hkl}) can optionally be applied, whereas the intensity of the reflectors (I_{hkl}) is only used as a threshold value to select the number of reflectors in the match unit.

2.3. Orientation

Orientation is recorded using the Euler angle convention (Euler 1775). Three Euler angles describe a minimum set of rotations that can bring one orientation into coincidence with another. During a measurement, this is the relationship between the EBSD detector and the particular point on the sample being measured under the beam. There is more than one convention but that of Bunge is most common. The three Euler angles: φ_1 , Φ , φ_2 represent the following rotations, which are shown schematically in Fig. 2.14.

1. A rotation of φ_1 about the z -axis followed by
2. a rotation of Φ about the rotated x -axis followed by
3. a rotation of φ_2 about the rotated z -axis.

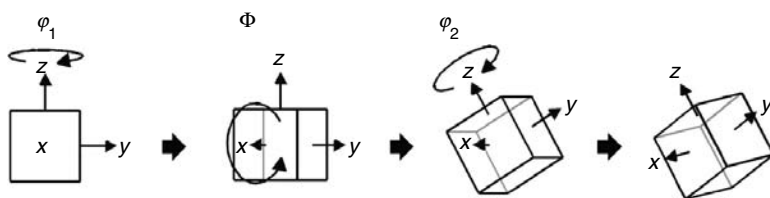


FIGURE 2.14. Euler angle rotations according to Bunge's convention. (Adapted from [13].)

2.4. Mean Angular Deviation

A number that expresses how well the simulated EBSD overlays the actual EBSD. The mean angular deviation (MAD) is given in degrees specifying the averaged angular misfit between detected and simulated Kikuchi bands.

2.5. Band Contrast

Band contrast (BC) is an EBSD quality factor derived from the Hough transform that describes the average intensity of the Kikuchi bands with respect to the overall intensity within the EBSD. The values are scaled to a byte range from 0 to 255 (i.e., low to high contrast). With this scale mapped to a grayscale from black to white, image-like maps can be plotted. These “images” show the microstructure in a qualitative fashion that were used to seeing either in the SEM or light microscope. Because EBSDs along grain boundaries tend to show poor BC they appear dark in a map. Conversely, EBSDs in undeformed regions of a grain appear light (see Fig. 2.15).

2.6. Band Slope

Band slope (BS) is an image quality factor derived from the Hough transform that describes the maximum intensity gradient at the margins of the Kikuchi bands in an EBSD. The values are scaled to a byte range from 0 to 255 (i.e., low to high maximum contrast difference), i.e., the higher the value, the sharper the band.

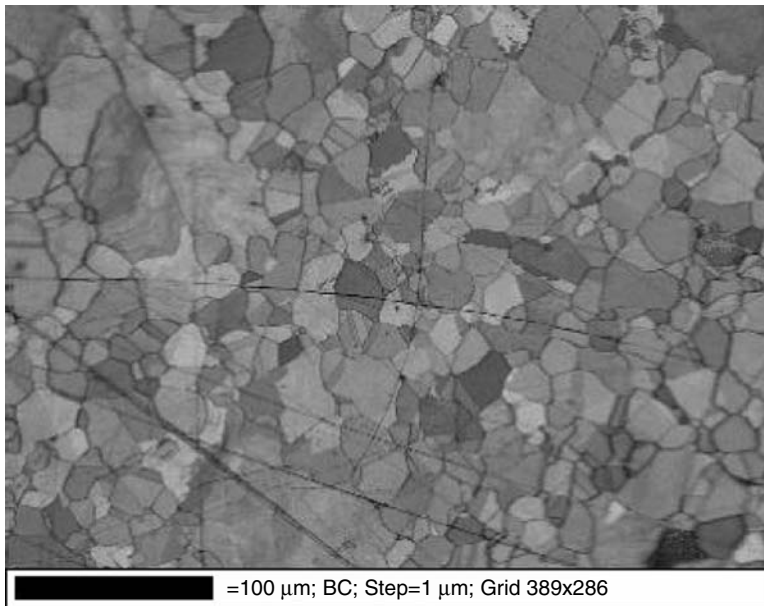


FIGURE 2.15. Band contrast map on Ni superalloy.

3. Data Analysis

Interrogation and analysis of the acquired data set is often performed away from the SEM with related data processing software that allows a great variety of analyses to be performed: grain size analysis, textural (preferred crystallographic orientation) analysis, and many modes of microstructural visualization and analysis with OMs.

3.1. Grain Size Analysis

EBSD grain size analysis uses changes in crystallographic orientation between neighboring grid points of greater than a defined minimum, typically 10° , to determine the position of grain boundaries (Figs. 2.16 and 2.17). Since the phase and orientation is known at each indexed point on the grid, the exact location and character of each grain boundary is known. Thus, certain grain boundary types such as twins or low-angle grain boundaries may be included or excluded, at the discretion of the analyst.

Classical linear intercept/grain segment detection analyses may be performed by the data processing software on map grids or by using dedicated line scans. Dedicated line scans allow large numbers of grain segments to be included in the analysis using a relatively short EBSD job time (<1 h), while still providing

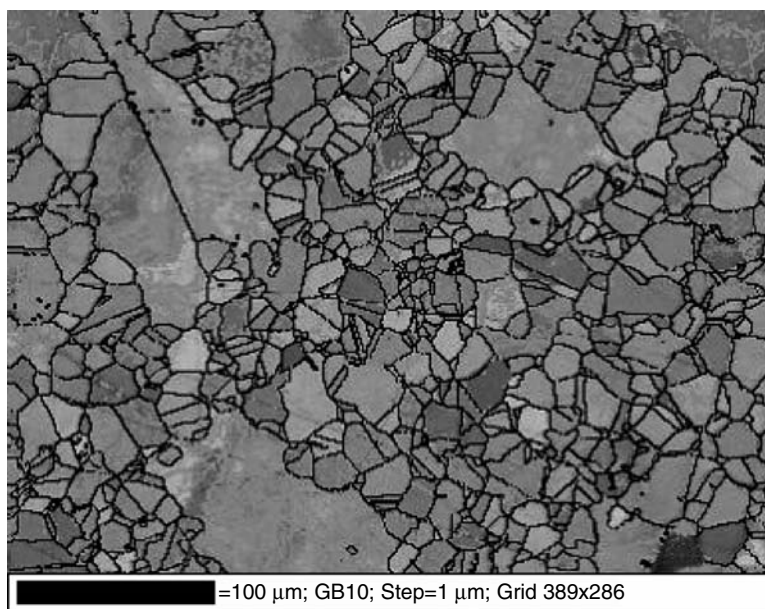


FIGURE 2.16. Band contrast map with 10° random grain boundaries shown as black 2 pixel-wide lines.

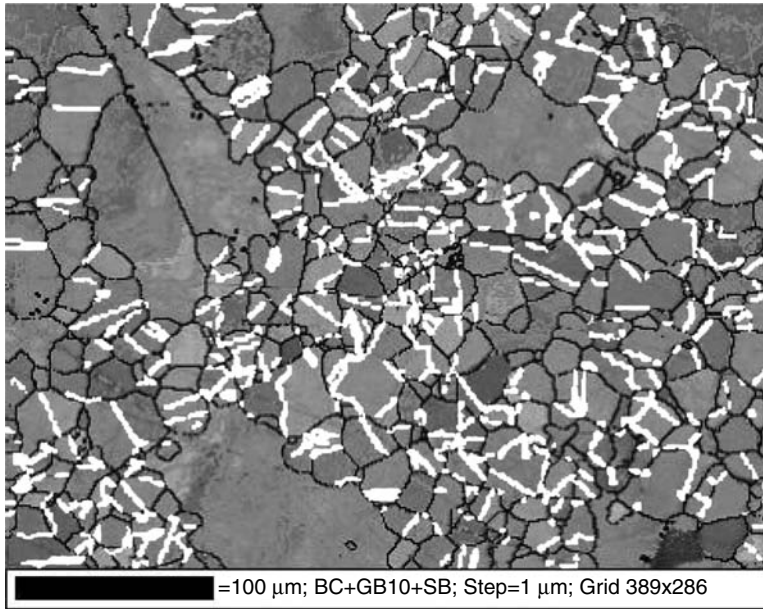


FIGURE 2.17. Band contrast, 10° random grain boundaries and white sigma 3 special boundaries (twins).

robust grain size statistics. Grain area determination from EBSD maps is a more comprehensive method of grain size and shape analysis. Here, the software determines the position of all grain-delimiting boundaries, again using the criteria specified by the operator, and calculates several characteristics of each grain, including area, equivalent circle diameter, aspect ratio (of a fitted ellipse), number of neighbors, and internal deformation by lattice rotation.

3.2. EBSD Maps

As with conventional SEM and optical imaging techniques, EBSD maps can be used to convey visually the basic character of the material's microstructure with 2D information about grain size and shape. However, because the phase and orientation at each pixel in the map is also known, EBSD data processing software can generate an enormous variety of additional visual and analytical information, including overall preferred orientation (texture), prevalence and distribution of grains in specific orientations, phase distribution, state of strain and local variations in residual strain, and character and distribution of grain boundaries.

Maps in EBSD are comprised of "components," or schemes used to color map pixels or boundaries between pixels based on the underlying data recorded. The properties used may be extracted from EBSD-derived properties of the pixel itself, properties of the local group of pixels to which the pixel in question

belongs (such as a grain), or information about the pixel by comparison to a neighbor or nonadjacent reference (such as its orientation relative to a reference orientation). In composing an EBSD map, the operator may choose a single component or mixture of components, the latter of which may be combined to form an additive color scheme, such as orientation coloring with the brightness or darkness controlled by the underlying pattern quality. The most commonly used components are pattern quality, phase, orientation, grain boundaries, special grain boundaries, and texture-related components. Other components are used when the material dictates, such as components for displaying state of strain. The basic components are described in more detail below.

3.2.1. Pattern Quality

The most typical is BC, a scalar value measured for each diffraction pattern collected regardless of index result. Essentially, BC is related to the brightness level of diffraction bands above a normalized background, and is affected by the diffraction intensity for a phase, dislocation/crystallographic defect density and orientation. Pattern quality maps are generally grayscale maps that appear similar to coarse SEM images, in part because every point on the map is assigned a brightness based on the pattern quality for that point. Grain boundaries are normally visible as low pattern quality (dark) linear features, and the highly sensitive orientation dependence of BC gives adjacent grains different grayscale values for a clear, SEM micrograph-like microstructural image at the resolution of the EBSD grid. Figure 2.15 is an example of a BC map.

3.2.2. Band Slope

Band slope (BS) is an alternative pattern quality parameter generated when band edge detection is used. This is a measurement of the intensity gradient at the edge of diffraction bands, as determined from peaks in Hough space. BS maps are not as clear as BC in depicting general microstructure because BS is not as sensitive to small orientation changes between grains, but it is more sensitive in general to the state of strain and has been used as a strain differentiator, e.g., to discriminate ferrite from near-cubic but deformed martensite in steels.

3.2.3. All-Euler Orientation Component

The All-Euler (AE) is a basic OM component that uses an Euler angle-based color scale. Euler angles are a set of three angles used to describe the crystallographic orientation of crystals relative to a reference coordinate system (usually defined by the primary SEM stage axes). Here, the value of each Euler angle is individually set to a color scale (normally red, green, and blue for Euler angles ϕ_1 , Φ , and ϕ_2 , respectively), and the three are combined into a single RGB color (see Fig. 2.18). In general, similar colors indicate similar orientations, so the AE-bearing OM is commonly used as a display of general microstructure, since the

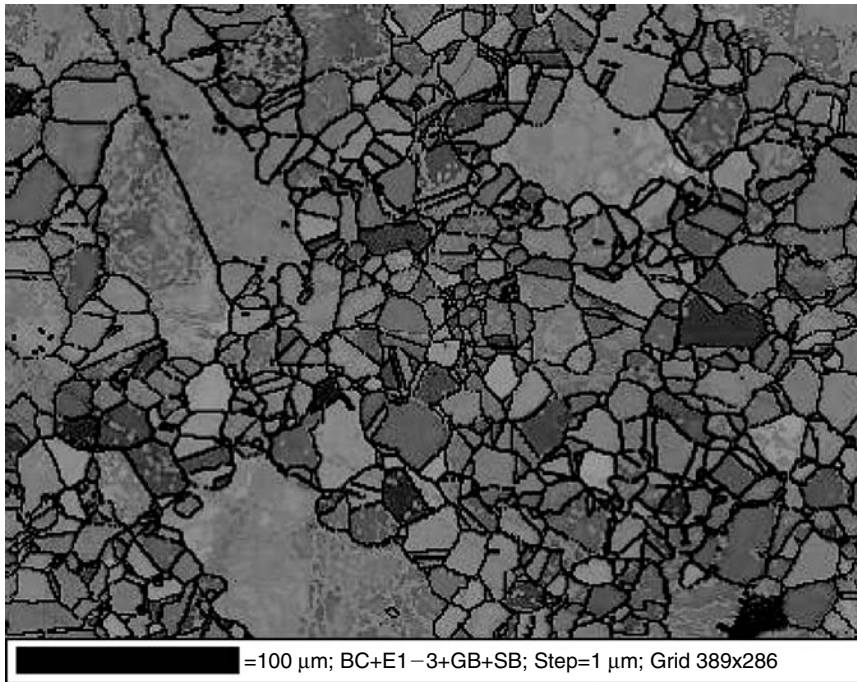


FIGURE 2.18. Ni superalloy showing grain boundaries and all-Euler coloring (see color insert).

basic grain structure and a general idea of strength of texture may be discerned at a glance. However, it is not intuitive to understand the relationship between specific colors and their corresponding orientations, and the AE component is subject to the “wraparound” effect. This happens when one or more of the Euler angles is near a limit, causing the R, G, or B component to vary between maximum and minimum, and showing color speckling where little or no actual orientation change exists. Because of these liabilities, some researchers prefer alternative coloring schemes for the primary EBSD display, most notably the inverse pole figure-based scheme, although all orientation coloring schemes have advantages and disadvantages.

3.2.4. Inverse Pole Figure

Inverse pole figure (IPF) orientation component uses a basic RGB coloring scheme, fit to an inverse pole figure. For cubic phases, full red, green, and blue are assigned to grains whose $\langle 100 \rangle$, $\langle 110 \rangle$ or $\langle 111 \rangle$ axes, respectively, are parallel to the projection direction of the IPF (typically, the surface-normal direction). Intermediate orientations are colored by an RGB mixture of the primary components, as seen in Figs. 2.19 and 2.20.

Although the IPF orientation map is not susceptible to “wraparound” color speckling as in the total Euler scheme, it has its own limitations. Most notable is

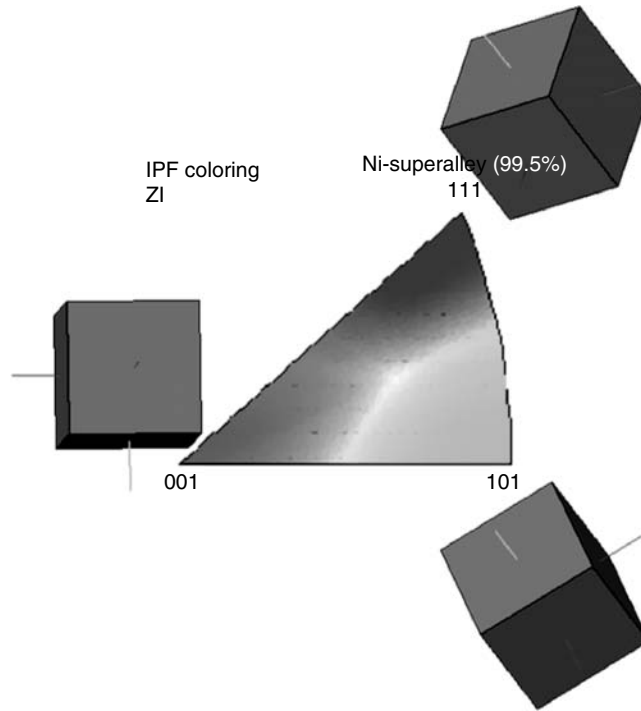


FIGURE 2.19. Inverse pole figure colored map (see color insert).

the coloring of pixels only by the projection-parallel crystallographic axis, independent of rotation about that axis. Thus grains with identical axes parallel to a specified IPF projection direction will have the same color in the IPF-based scheme, but may be in significantly different orientations. For example, two grains with $\langle 100 \rangle$ parallel to the surface normal are both colored red, but possess 30° of relative rotation about that axis. IPF-based orientation maps are most useful for displaying materials with strong fiber-textures and for understanding preferred orientations parallel to a sample direction of interest.

3.2.5. Texture Component

Texture component (TC) map is another OM component, but unlike AE and IPF, TC employs a user-determined orientation coloring scheme relative to a specific orientation of interest. Texture components use ideal orientations as references and color each pixel on a map relative to the misorientation between the orientation at that point and the reference. The reference may be set by the analyst to a fiber-texture definition, crystallographic definition (e.g., plane/direction pair), or a set of Euler angles from any point on the map. Commonly, a rainbow scale is

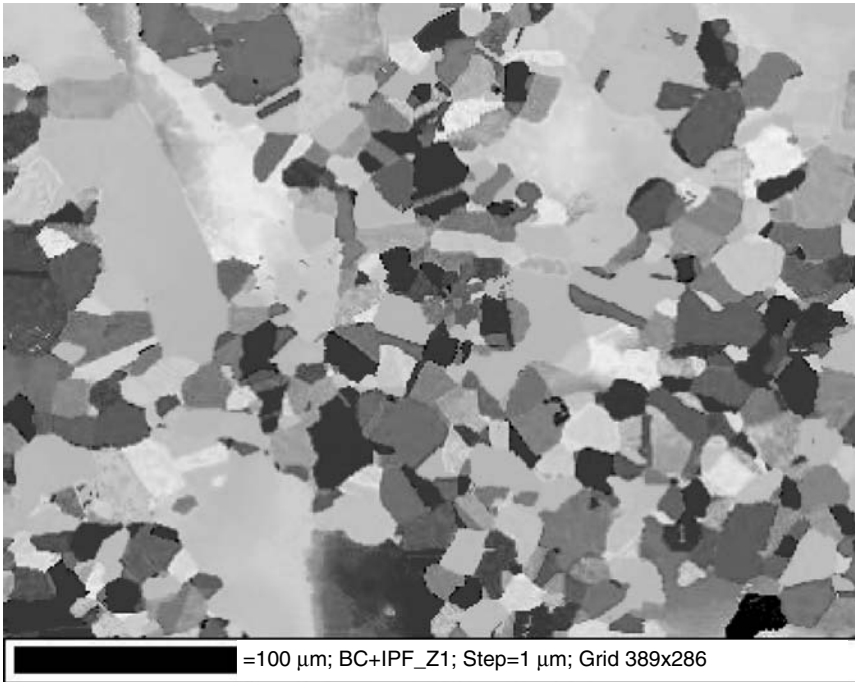


FIGURE 2.20. Surface normal-projected inverse pole figure orientation map (see color insert).

fit to the range of misorientations, the maximum of which may be set by the analyst. These components are used to visually and quantitatively understand the conformity between orientation in the sample and an orientation of interest to the analyst, for example, a deformed primary grain's orientation is the reference and the recrystallized daughter grains within the deformed grain are colored by degree of closeness to that orientation.

3.2.6. Grain Size Coloring Component

Entire grains are colored by their size relative to the range of grain sizes in the map, commonly using a rainbow scale. As with all grain size-related functions in EBSD, the analyst may include or exclude any grain boundary type, such as special boundaries (CSLs, twins) and/or subgrain boundaries, in the grain size analysis and resulting grain size map. An example of the usefulness of this map is in grain reconstructions in Cu thin films for the electronics industry. Here, annealing twins may be disregarded and the nontwinned microstructure revealed and analyzed.

3.2.7. Grain Internal Misorientation Component

Here, grain boundaries are determined and orientation relationships *within* grains are analyzed. Intragranular lattice rotation is a common response of many materials to deformation. It is an expression of plastic strain where dislocation recovery has occurred, forming subcells, and if the subcell size is approximately within the spatial resolution of the SEM and EBSD system, the resultant small changes in orientation may be visualized and analyzed quantitatively. Although the degree of rotation between neighboring pixels depends on the step size used in the EBSD grid as well as the intragranular rotation in the sample, cumulative rotations may be discerned. There are several variations of this map, using different measures of intragranular lattice rotation. Two of the most common are: (a) the kernel-type, whereby each pixel in the map is colored as a function of the degree of orientation change with respect to its neighbors; and (b) the coloring of pixels within grains by the degree of their rotation with respect to a reference orientation within the grain. Quantitative strain analysis by EBSD is not yet common in the materials and geology communities, but studies have shown that this measurement is a strong indicator of degree of plastic strain, and with certain limitations quantitative strain analysis by EBSD may be possible.

3.2.8. Grain Boundary

Grain boundary (GB) component draws grain boundaries between map pixels where there is an interpixel change of orientation greater than an user-defined minimum, usually 2–5° this is because the angular resolution of the technique is limited to ~0.5 at best. When mapping a sample at high speed, this limit may be higher and in some cases reach several degrees. Typically, grain boundaries with misorientations between 2° and 10° are considered subgrain or low-angle grain boundaries and given a specific color, such as silver, whereas boundaries with misorientations >10 are considered random high-angle grain boundaries and are typically colored black. Tools allow percentages of grain boundaries in each category to be compared, and maps possessing this component allow the concentration and distribution of low angle grain boundaries to be determined. If the neighboring pixels are from different phases, phase boundaries may be displayed instead.

3.2.9. Special Boundaries

Special boundaries (SB) are individual user-defined boundaries using an axis-angle definition to identify specific types of boundaries. For example, the $\Sigma 3$ CSL/twin typical in copper and nickel-base alloys may be described by a 60° rotation about $\langle 111 \rangle$ between neighboring crystallographic domains. Tools are also available to determine the character, prevalence and distribution of special boundaries where the axis/angle definition is not known for a material or processing method.

Most of these map types are demonstrated in the section “Applications.” Quantitative analysis of the information depicted in an EBSD map is also usually possible. For a map made of a mixture of pattern quality and grain size coloring

components, histograms may be generated describing the overall frequency distribution of the pattern quality parameter, as well as the grain size distribution within the area of analysis. Numbers and percentages of grains and grain areas within different ranges of grain size are easily extracted. These histograms can also display the coloring scheme used for the range of values in the map.

Subsetting is another powerful tool of EBSD, in which selected areas of maps, ranges of measured values or ranges of orientations may be extracted from the complete set of data and independently analyzed and compared. For example, if the grain size analysis indicates a bimodal grain size distribution, the two populations can be analyzed separately with any of the texture or mapping tools available.

4. Applications

Five applications examples are presented, two on samples with grain sizes on the micron-scale, and three with grain sizes on the nanometer scale. The micron-scale group is presented to demonstrate some of the unique analytical capabilities of the technique on strained samples: a strained aluminum alloy and a strained Fe–Al intermetallic alloy, using mapping grid resolutions of 0.7 and 1.0 μm , respectively. The nm-scale group includes samples with grain sizes on the order of tens to hundreds of nanometers: a Pt thin film, a Cu thin film pattern, and an Al thin film using 5, 5 and 10 nm grid resolutions, respectively.

4.1. Friction-Stir Welded Aluminum Alloy

A friction stir welded aluminum alloy (AA2024) was cross-sectioned, polished, and analyzed by EBSD. This analysis used a 772×235 point grid at 0.7 mm steps, placed on the interface between the “nugget” and thermo-mechanically affected zone (TMAZ).

Figure 2.21 is a basic OM with grain boundaries; the “nugget” region is the finer-grained area on the left, the TMAZ is the coarser-grained area on the right. Grain size analysis of these areas gives an average of 4.9 and 13.5 μm , respectively. The orientation colors are related to the surface normal-projected IPF, again where points on the sample with a $\langle 111 \rangle$ axis parallel to the surface normal are blue, $\langle 110 \rangle$ green, $\langle 100 \rangle$ red (see legend) and intermediate orientations have intermediate colors. The variety of colors in the map implies no significant surface-normal parallel texture, verified by the contoured IPF for this projection direction. However, inspection of the orientation distribution function (ODF) indicates a strong brass texture (Fig. 2.22). Grain boundary character and distribution on this map give an indication of the strain state difference between the “nugget” and TMAZ. The TMAZ grains possess considerable subcell structure, indicated by the presence of subgrain boundaries in silver. In contrast, the “nugget” grains are relatively free of subgrain boundaries, with few grains subdivided by silver lines.

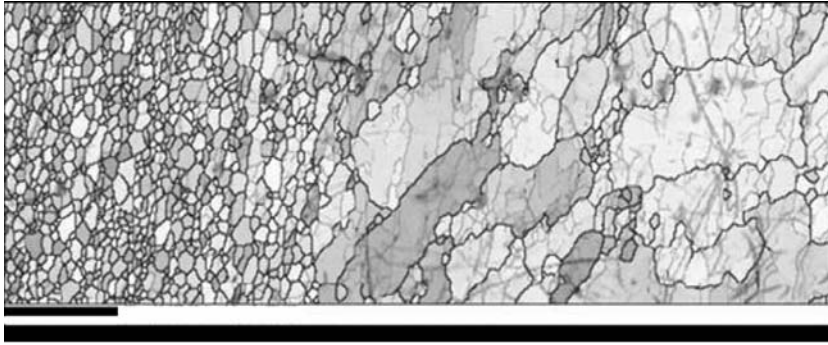


FIGURE 2.21. All euler map of Friction Stir Welded Al AA2024 showing advancing side microstructure. The “nugget” region is the fine grained area left, the TMAZ is the coarser grained area on the right. Scale bar = 100um.

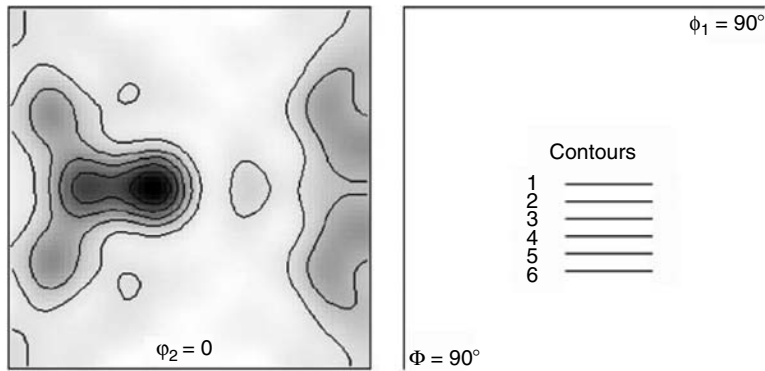


FIGURE 2.22. Slice of ODF at $\phi_2 = 0^\circ$. Strength and position of contouring indicates strong brass texture.

A map containing an intragranular lattice rotation-based strain analysis component is displayed in Fig. 2.23. Here, the EBSD postprocessing software detected grains, found the most logical reference point within each grain, and colored every pixel by the degree of orientation change (rotation) relative to the orientation of the reference pixel for that grain. The coloring scheme is a blue-to-red rainbow scale, with blue indicating orientations closest to the reference, red furthest, and the range set by the maximum for the map, in this case. The map shows that the TMAZ grains contain a wider variation in color than most “nugget” grains, indicating a higher state of strain on an average, and an interesting subcell structure within the TMAZ grains, bounded by the silver subgrain boundaries. Note that in general it is not known if smaller grain sizes cause seemingly lower degrees of indicated deformation in this type of map, either because of smaller volume per grain or different deformation mechanisms (such as grain boundary

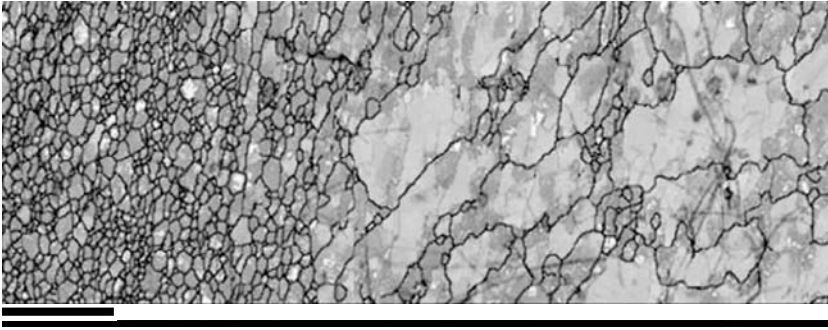


FIGURE 2.23. Grain internal deformation map, based on intragranular lattice rotation relative to a reference point in each grain. Coloring scheme follows a rainbow scale, where blue = smallest rotation from reference orientation, red = 10° of rotation. Scale bar = $100\ \mu\text{m}$ (see color insert).

sliding). However, examinations of strained samples with a range of grain sizes have not yielded a clear correlation between grain size and average intragranular misorientation.

4.2. Deformed Fe–Al Intermetallic Alloy

This example is a single-phase alloy that has been cast, extruded, hot rolled, and cold rolled by 80%. It contains two populations of grains, deformed, and recrystallized, which are differentiated by grain size, orientation, and state of strain. The EBSD mapping used a 563×1097 point grid at $1\ \mu\text{m}$ steps.

Figure 2.24 is a basic BC map with grain boundaries where high angle ($>10^\circ$) boundaries are black, low angle red, and very low angle yellow. The two populations

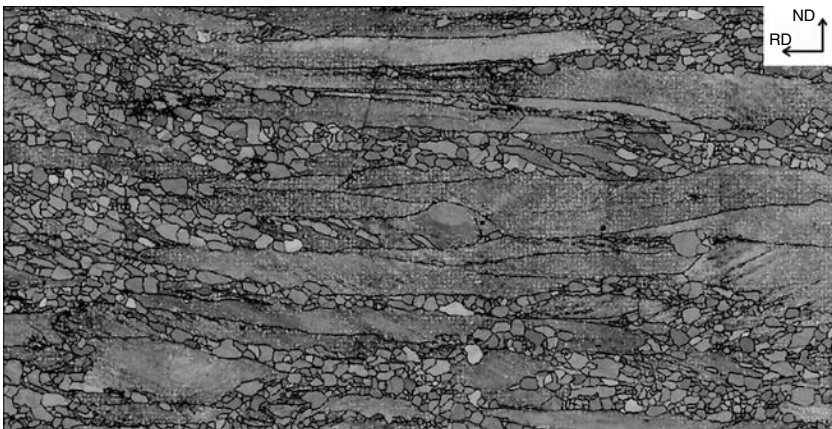


FIGURE 2.24. Pattern quality (band contrast) map, high angle boundaries in black, low angle grain boundaries in red, very low angle in yellow. Vertical black scale bar on right = $200\ \mu\text{m}$ (see color insert).

can be clearly seen in smaller equant grains between large, elongated grains. The abundance of red and yellow boundaries within the larger (deformed) grains and lack of same in the smaller (recrystallized) grains is one indication of a higher degree of strain-related substructure in the deformed grain population.

For Fig. 2.25, all grains have been classified as deformed or recrystallized, in red and blue, respectively. To do this, the EBSD software determines the average intragranular orientation spread for each grain; the larger this metric for an individual grain, the more substructured the grain is and the more residual strain the grain may be assumed to contain. In the case of this EBSD job, examination of the frequency spread of this value clearly indicated the two populations, and each grain was thus classified. Grain size could also have been used here, but for any given sample, grain size alone may not be a good discriminating factor. Once the grains are classified into a subset, other comparative analyses may be performed, such as area percentage and texture. Here, the recrystallized grains make up 31% of the area of analysis. Comparison of the degree of preferred orientation is shown in the pole figures in Fig. 2.26. Figure 2.27 shows an IPF-based OM, where the IPF projection direction is parallel to the rolling direction (RD). Immediately noticeable is the relative variety of coloring in the smaller grains, implying a weaker or nonexistent preferred orientation, whereas the larger grains have a greenish hue, indicating a stronger $\langle 110 \rangle \parallel \text{RD}$ fiber texture and corroborating the RD-parallel $\{110\}$ peak for the deformed grains in the $\{110\}$ pole figure.

4.3. Platinum Thin Film

This experiment characterized a small section of a Pt thin film on a Si substrate (with intermediate SiO_2 and TiO_2 layers), with tens-of-nanometer scale Pt grains. A thermal FE-SEM was operated under high resolution, low probe current

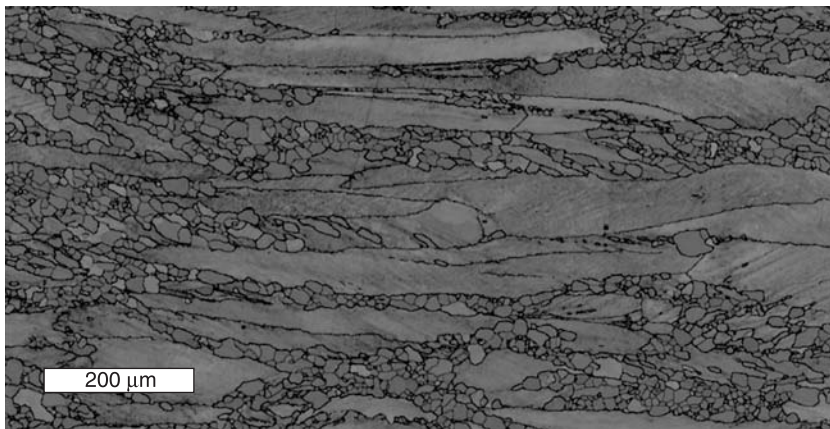


FIGURE 2.25. Map with two classifications of grains: red = deformed, blue = recrystallized, based on degree of internal lattice rotation. High angle grain boundaries are also shown in black. [Adapted from [14].] (see color insert).

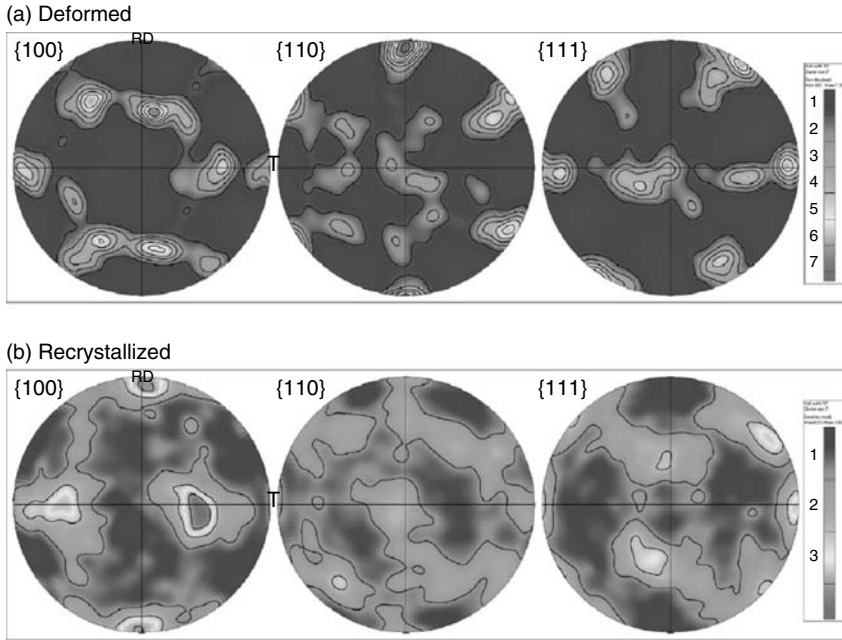


FIGURE 2.26. (a) and (b) Contoured pole figures for the deformed and recrystallized grains, respectively, shown in Fig. 2.25.

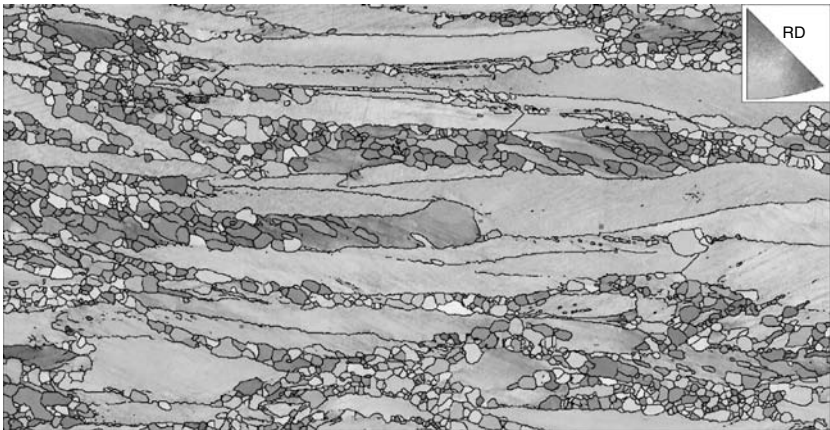


FIGURE 2.27. Rolling direction-projected IPF-based map. Green deformed (large, in this case) grains indicate a strong $\langle 110 \rangle$ RD texture not shared by the smaller recrystallized grains. Vertical black scale bar on right = 200 μm .

conditions (25 kV, 0.5 nA) at a fairly small working distance (10 mm) to achieve the required spatial resolution. Further, a high sensitivity digital detector was used. The EBSD grid was 50×50 at 5 nm steps.

Figure 2.28a is a pattern quality map of the acquisition area, showing the mostly equiaxed microstructure. Grain boundaries are seen as low pattern quality (darker) regions surrounding higher pattern quality grain cores.

An IPF-based OM is given in Fig. 2.28b projected parallel to the surface normal, with high angle grain boundaries in black and low angle ($2\text{--}10^\circ$) boundaries in silver. The preponderance of blue in the map indicates a strong $\langle 111 \rangle \parallel$ surface normal texture, and the lack of consistent coloring in the X-projected (Fig. 2.28c) and Y-projected (Fig. 2.28d). IPF-based maps all indicate that this is a surface normal-parallel *fiber* texture, meaning there is no strongly preferred (rotational) orientation about the primary $\langle 111 \rangle$ texture peak. The surface normal-normal-projected IPF and $\{111\}$ pole figures in Fig. 2.29 corroborates a $\langle 111 \rangle \parallel$ surface normal fiber texture.

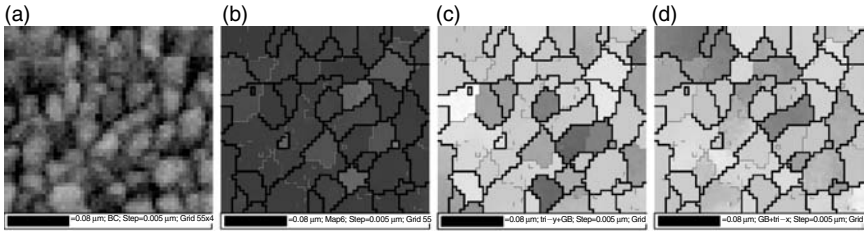


FIGURE 2.28. EBSD maps of Pt thin film. (a) Band contrast (pattern quality) map showing basic grain structure independent of indexing; (b) surface normal-projected IPF-based orientation map, blue color indicating strong $\langle 111 \rangle \parallel$ surface normal texture; (c) and (d) are surface plane horizontal and vertical-projected IPF maps, respectively, and show no strong texture in these directions. Scale bar = 80 nm. (Adapted from [15].) (see color insert).

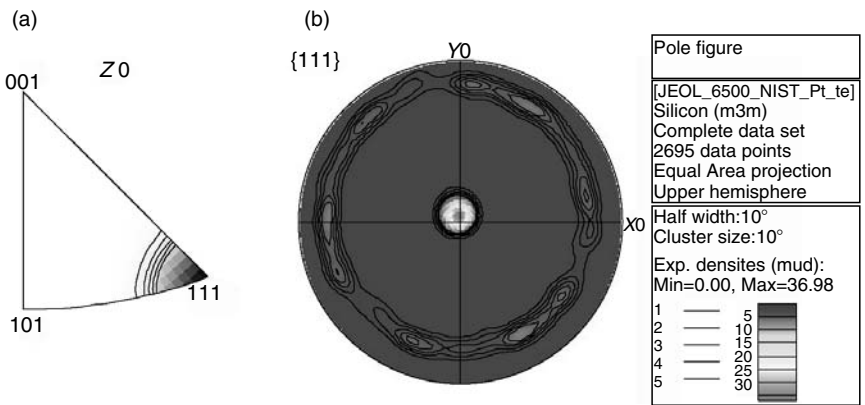


FIGURE 2.29. (a) Surface normal-projected IPF and (b) $\{111\}$ pole figures, showing strong $\{111\} \parallel$ surface normal texture. (Adapted from [15].)

The ODF also indicates close compliance of the texture in this area with the $\{111\} \parallel$ surface normal (gamma) fiber texture definition. ODFs are 3D representations of “Euler space,” with the three Euler angles (φ_1 , Φ , and φ_2) that describe the orientation of a crystal forming the axes. A crystal’s orientation is represented as a point within that space. Although not as intuitive to most analysts as the conventional pole figure, the ODF may more clearly reveal subtle and compound textures. Figure 2.30a gives the contoured (coefficient) for this job, showing the strongest texture in a tube-like feature close to centered on the $\Phi - \varphi_2$ plane and elongated parallel to the φ_1 Euler angle, corresponding with the gamma-fiber texture. Offsets between the actual and ideal peak concentration positions, as well as variations in intensity along the length of the tube, can be used to understand the actual texture peak orientation and clustering of orientations within the gamma fiber texture definition, respectively. Figure 2.30b shows a $\Phi - \varphi_1$ cross section, which is a slice along the length of the gamma fiber “tube.” The nonuniformity along the length of the “tube” cross section indicates some rotational orientation clustering about the texture peak. These features of the ODF correspond with the peak offset seen in the pole figure in Fig. 2.29b and the nonuniform $\{111\}$ peak distribution in the ring structure in the pole figure. These conclusions, however, are primarily for demonstration, as the grain sampling in this job is too small for a statistically valid textural analysis.

Although grain boundary positions in this map correspond with the positions of anticipated grain boundaries in the BC map, many are low-angle grain boundaries, colored green (Fig. 2.31). See for example the relatively large grain just to the left and below the center of the map. The BC information seemingly clearly shows that this area comprises 6–7 separate grains; however, the low angle grain boundaries in the OM reveal the orientation relationships between neighboring grains in this area to be $<10^\circ$, forming a typical subgrain-divided primary grain. Although strong fiber textures (strongly preferred orientation of a single crystallographic axis) constrain the possible range of disorientations between grains, increasing the likelihood that random neighboring grains will have low-angle

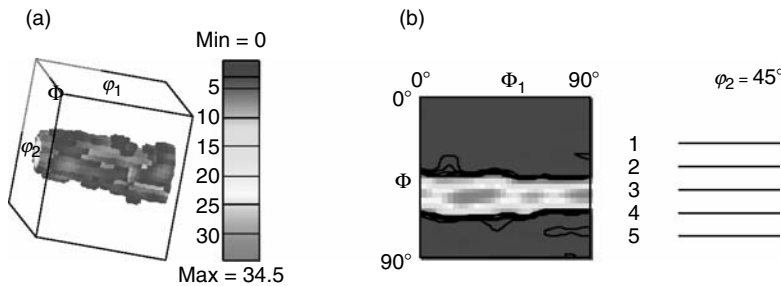


FIGURE 2.30. (a) Orientation distribution function (ODF) coefficient. Tube-shaped feature parallel to φ_1 indicates strong $\langle 111 \rangle \parallel$ surface normal texture. (b) $\Phi - \varphi_1$ parallel slice through ODF at $\varphi_2 = 45^\circ$. Discontinuities along “tube” length may be analyzed to detail preferred orientations about $\langle 111 \rangle$ within the primary fiber texture. (Adapted from [15].)

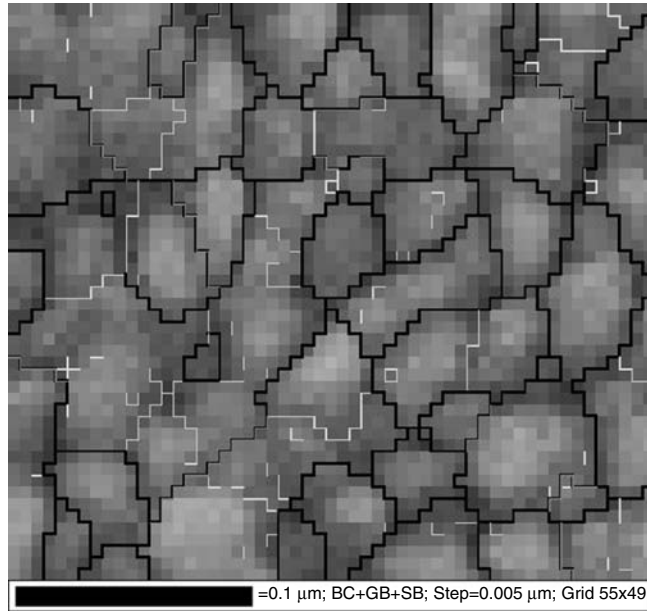


FIGURE 2.31. EBSD map of Pt thin film showing high-angle and low-angle grain boundaries in black and white respectively. Note step size of 5 nm shows that grains of size down to 20 nm in diameter (4 pixels) can be reliably distinguished.

grain boundaries between them, in cubics the $\langle 111 \rangle$ fiber texture definition allows the maximum range of 60° for grains to perfectly conform to the textural definition.

Disregarding low angle grain boundaries but including the $\Sigma 3$ twins (red grain boundaries in Fig. 2.31) as grain-delimiting boundaries, EBSD grain size analysis in this small area revealed 16 grains with a 35 nm grain equivalent-circle diameter average.

4.4. Copper Thin Film

EBSD analysis of thin film copper sheets and interconnects comprises an important and growing segment of modern EBSD use. As the width of interconnects is miniaturized below the single-grain scale, grain boundary character, grain size, and overall texture become increasingly important factors dictating circuit life in service. Each of these characteristics are easily extracted and examined with EBSD. In this example, a set of 500 nm-wide copper lines is examined at two EBSD resolutions, using a thermal FEG-SEM operated at 20 kV, with 1 nA probe current and a 5 mm working distance.

Two jobs are discussed here. The first job used a 537×770 point grid at 20 nm steps. Figure 2.32 is an All-Euler OM with random high-angle grain boundaries in black and $\Sigma 3$ CSLs in red. This shows a typical annealing-twinned copper



FIGURE 2.32. All-Euler orientation map with grain boundaries. Most grains are heavily twinned and span the length of interconnect lines. Drawn box shows location of higher-resolution run. Scale bar = 2 μm (see color insert).

structure, with single grains spanning entire interconnect widths. A strong gamma-fiber ($\langle 111 \rangle \parallel$ surface normal) texture is seen in the pole figure set in Fig. 2.33.

Figures 2.34 and 2.35 are grain size maps, in which the smallest detected grains are colored blue, the largest red, and intermediate-sized grains colored with intermediate rainbow colors. Figure 2.34 shows the crystal domain structure using this method where all twins are counted as grain-delimiting boundaries. Figure 2.35 ignores these boundaries in detecting grains, and the resultant “bamboo” structure is revealed, with most grains much larger than interconnect widths, incorporating multiple twin domains.

A second acquisition job was run in this area at a 5 nm step size, using a 395×385 point grid. Although some drift/instability caused the lines to appear wavy, the grain and twin domain structures are revealed. Figure 2.36a is a pattern quality map showing the general grain structure and position of grain boundaries. The

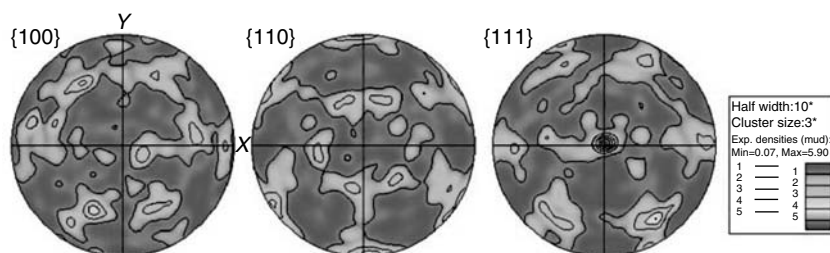


FIGURE 2.33. Contoured pole figure set, displaying strong $\langle 111 \rangle \parallel$ surface normal texture (see color insert).



FIGURE 2.34. Grain size (equivalent-circle diameter) map, with all $\Sigma 3$ twins as grain-delimiting boundaries. Scale bar = 2 μm (see color insert).

All-Euler OM in Fig. 2.36b gives the nature of these boundaries, with all boundaries on the right interconnect in red (twins), and a pair of relatively small grains in the left interconnect bounded by a black (random) high angle grain boundary. The green grain in this pair has grain boundaries in the positions expected from

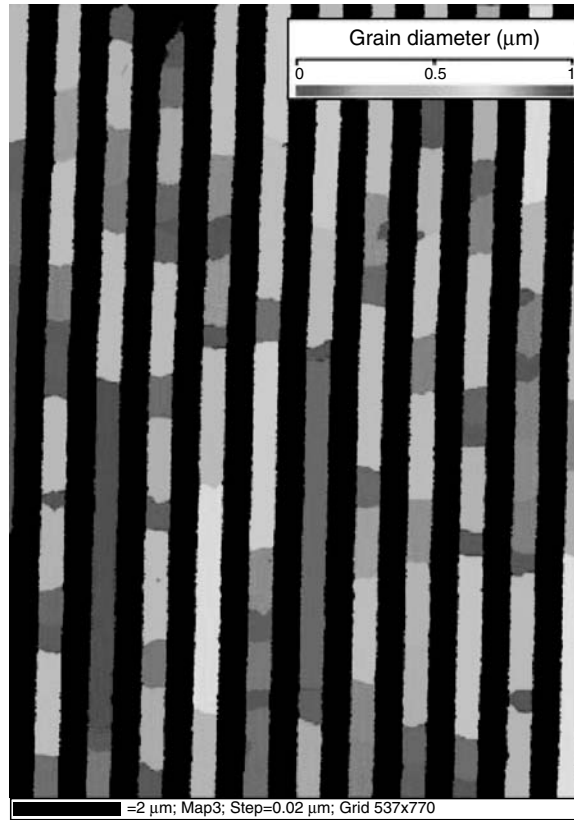


FIGURE 2.35. Grain size (equivalent circle diameter) map, disregarding $\Sigma 3$ twins as grain-delimiting boundaries. Scale bar = 2 μm (see color insert).

the pattern quality map, but one of them is a finely divided twin domain, the other a low angle grain boundary. Note that twin domains <30 nm wide are resolved in this map.

4.5. Aluminum Thin Film

EBSD data acquisition on this 100 nm-thick film used a thermal FEG SEM operated at 10 kV. Fine-grained aluminum presents a special challenge compared to platinum and copper because of its lower density and lower electron scattering efficiency, impacting both spatial resolution and acquisition speed. Since drift is commonly a factor in high-resolution EBSD, a fast acquisition rate was necessary, so a relatively high beam current (>5 nA) was used at the expense of spatial resolution. These conditions, along with the high sensitivity digital detector, allowed data acquisition in a minimum of time to mitigate the effects of drift. This job used a 500×400 point grid at 10 nm steps.

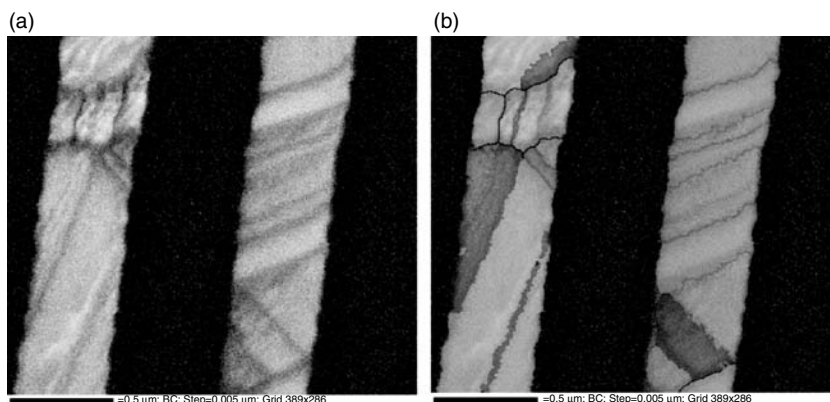


FIGURE 2.36. (a) Pattern quality (band contrast) map; (b) All-Euler orientation map. Waviness due to instability during acquisition. Note <30 nm twin domain at bottom of left interconnect. Scale bar = 500 nm (see color insert).

The pattern quality map in Fig. 2.37 shows a fine-grained microstructure, with a large proportion of the map dark, indicating poor pattern quality likely associated with a relatively large probe and electron scattering at grain boundaries. The larger grains in the mapping area show as higher pattern quality “islands.” Visually, the higher pattern quality grains are ~100 nm in diameter.

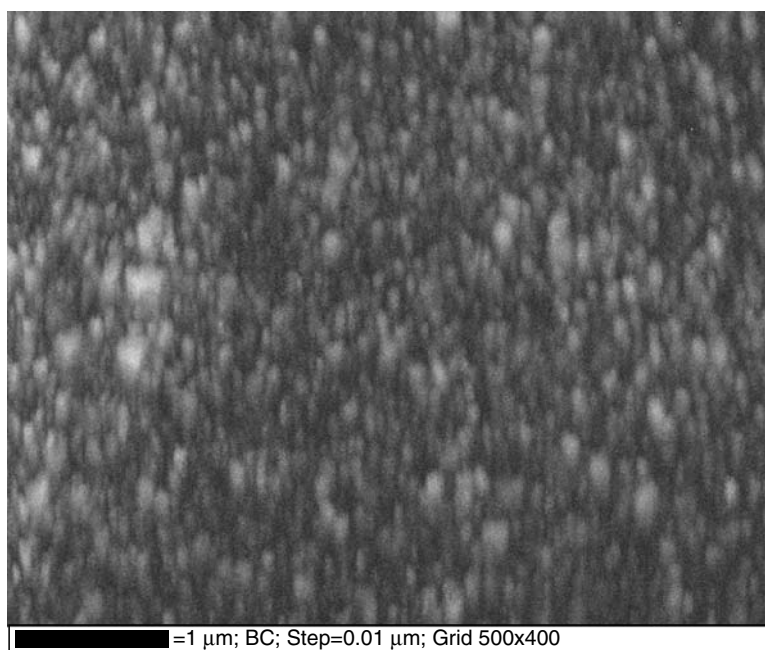


FIGURE 2.37. Pattern quality (band contrast) map, showing higher pattern quality grain cores and lower pattern quality (darker) finer grained regions.

Figure 2.38 is a surface normal-projected IPF map. As with the other metal films discussed in this chapter, blue grains are dominant indicating a strong $\langle 111 \rangle \parallel$ surface normal texture. Again, the pole figures in Fig. 2.39 corroborate this, and a comparatively uniform $\langle 111 \rangle$ ring at 70° from the texture peak indicates good compliance to the ideal gamma fiber texture.

Figure 2.40a further examines this texture. Here, grains with $\{111\}$ poles within 20° of the surface normal are plotted in color, all others are colored in the

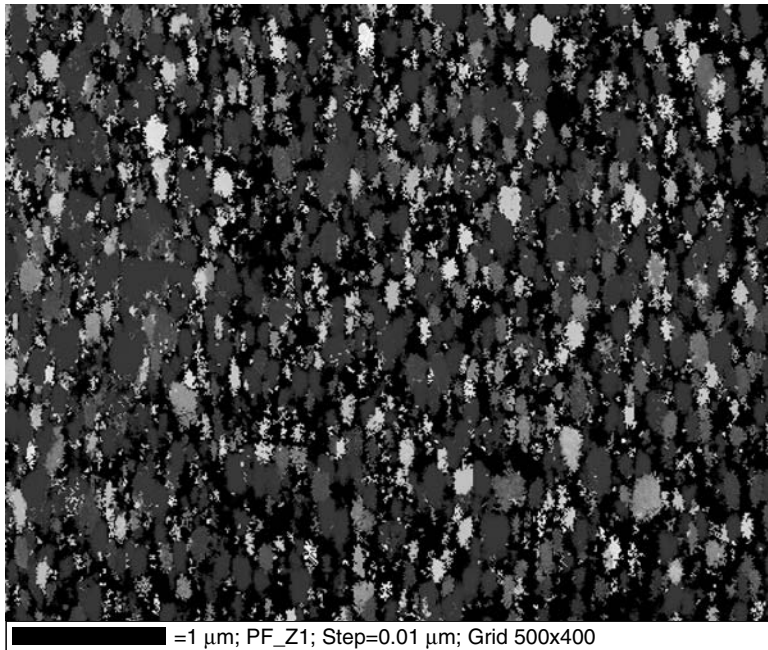


FIGURE 2.38. Surface normal-projected IPF-based orientation map, legend in Fig. 2.17. Predominance of blue grains implies a strong $\langle 111 \rangle \parallel$ surface normal texture (see color insert).

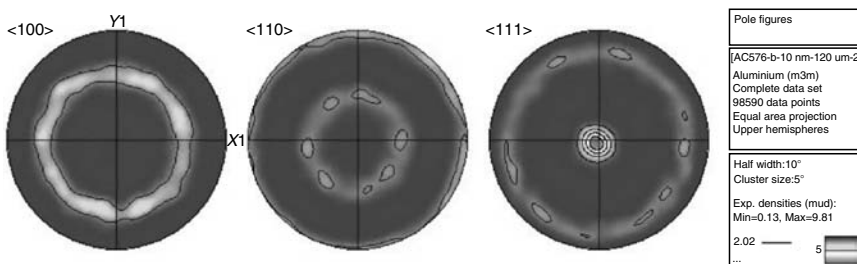


FIGURE 2.39. Standard cubic pole figure set, contoured, showing strong $\langle 111 \rangle \parallel$ surface normal fiber texture.

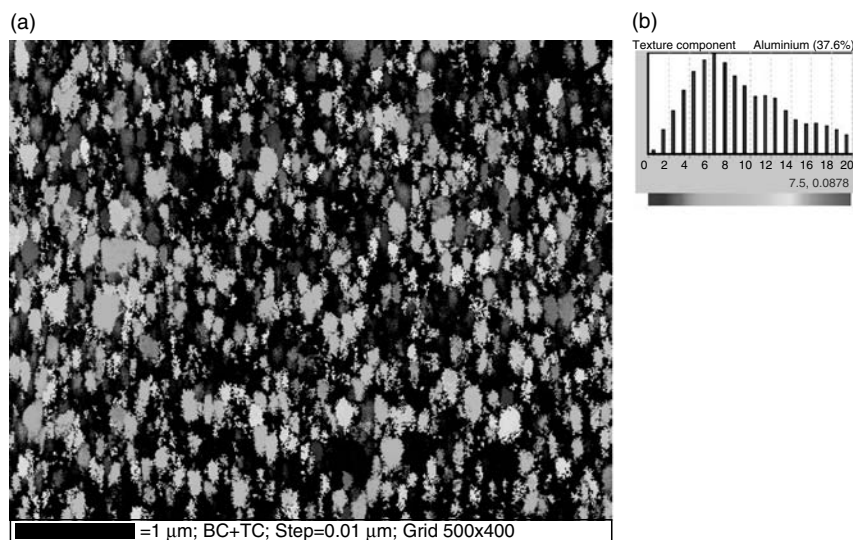


FIGURE 2.40. (a) Orientation map with grain coloring by degrees of misorientation relative to a perfect $\langle 111 \rangle \parallel$ surface normal parallelism, with blue = closest to parallel, red = 20° from parallel. (b) Legend showing rainbow scale fitted to $0\text{--}20^\circ$ range (see color insert).

background pattern quality grayscale. Grains oriented most closely to the ideal texture are colored blue, others are colored along the rainbow scale to red with increasing misorientation. The legend, Fig. 2.40b, shows a histogram of the distribution of this misorientation, and indicates that 38% of the map area is within 20° of the ideal orientation.

5. Current Limitations and Future

5.1. Spatial Resolution

At present, spatial resolution of this technique is limited to grain sizes of ~ 20 nm in diameter. This assumes that a map is created at a sampling step size of 5 nm, and therefore is reasonably conservative in needing 4 pixels to represent a 20 nm grain diameter. The spatial resolution is primarily determined by the SEM and geometry of the sample/lens/EBSD detector relationship. As FE-SEM resolution has improved, so has the minimum grain size visible in EBSD maps. With the advent of aberration corrected FE-SEMs, a concomitant benefit in resolution should be seen.

5.2. Angular Resolution

Angular Resolution is presently limited to $\sim 0.5^\circ$. This is dictated by the resolution of the EBSD detector and its position with respect to the sample. Although it is possible to operate at this resolution, current cameras sacrifice speed for additional angular resolution. Since most standard textural analyses need only to resolve a few degrees to determine a grain boundary, the need for improved angular resolution might only be required for strain and small lattice rotation measurements.

5.3. Speed

Speed has improved greatly over the years since automatic mapping was introduced. Speeds of up to 100 indexed points per second are now achievable on well-prepared cubic materials. It is expected that advances in camera design will allow mapping speeds to continue to increase.

6. Conclusion

EBSD is a powerful, quantitative SEM technique that has moved from the province of university materials and geology departments to industrial production control. While its penetration has yet to reach its full potential, the technique is well on the way to becoming yet another detector situated on the chamber of an SEM.

References

1. T. M. Maitland, unpublished work (2005).
2. Figures 2.2–2.4, assistance of Robert Schwarzer is gratefully acknowledged.
3. K. Shinohara, *Sci. Pap. Inst. Phys. Chem. Res.*, 20 (1932/1933) 39.
4. Boersch *Physikalische Zeitschrift*, 38 (1937) 1,000.
5. M. N. Alam, M. Blackman, and D. W. Pashley, *Proc. Roy. Soc.*, 221(1954) 224.
6. D. C. Joy and G. R. Booker, *J. Phys. E: Sci. Instrum.*, 4 (1971) 837.
7. D. J. Dingley, *Proc. Roy. Microsc. Soc.*, 19 (1984) 74.
8. J. A. Venables and C. J. Harland, *Phil. Mag.*, 27 (1973) 1193.
9. Used with kind permission of Prof. Val Randle, University of Swansea.
10. P.V.C. Hough, US Patent 3069654 (1962).
11. A. Queisser, *C/C++ Users Journal*, December 2003.
12. Courtesy: Professor Dave Prior, University of Liverpool.
13. A. P. Day et al., *Channel 5 User Manual*, HKL Technology A/S, Hobro, Denmark (2001).
14. P. W. Trimby et al., *Applications Catalogue*, HKL Technology A/S, Hobro, Denmark (2001, 2003).
15. X. D. Han, S. Sitzman, and T. M. Maitland, unpublished work (2005).

Scanning Microscopy for Nanotechnology
Techniques and Applications

Zhou, W.; Wang, Z.L. (Eds.)

2007, XIV, 522 p. 399 illus., Hardcover

ISBN: 978-0-387-33325-0